

pubs.acs.org/cm Article

Microstructurally Strained Pyrochlore—Perovskite Biphasic Electrocatalysts for the Oxygen Evolution Reaction

Bidipta Ghosh, Gavin S. Lindsay, Sohini Mandal, Toby Woods, Qian Chen, Andrew A. Gewirth, and Hong Yang*



Cite This: Chem. Mater. 2025, 37, 7687-7699



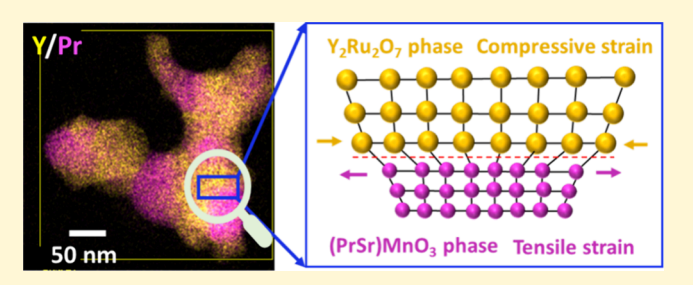
ACCESS I

III Metrics & More

Article Recommendations

Supporting Information

ABSTRACT: Efficiency of water splitting for hydrogen production is often limited by the sluggish kinetics of multiple electronic transfers required in the heterogeneous oxygen evolution reaction (OER). Catalyst design for reducing the high OER overpotential remains a major scientific challenge. Lattice-strain engineering, a method for tuning the electronic structure and surface geometric configuration of active sites, may greatly affect the interaction between adsorbates and catalytic surfaces for high activity and stability. In this study, we present the synthesis of biphasic oxides of YPrSrRuMnO $_{xy}$, which consists of distinct phases of Y $_2$ Ru $_2$ O $_7$



pyrochlore and (Pr_{0.7}Sr_{0.3})MnO₃ perovskite, and the development of a suitable analytical approach to study the strain—catalytic property relationship. Linear sweep voltammetry results reveal that the biphasic oxide exhibits approximately 3.1 times greater mass activity and 2.4 times larger turnover frequency (TOF) than single-phase Y₂Ru₂O₇ in the 0.1 M HClO₄ electrolyte. The biphasic catalyst is also about 3 times more stable than the single-phase oxide under acidic conditions. X-ray photoelectron spectroscopy, nitrogen isotherm, and electrochemical surface area analyses indicate that the oxidation state, specific surface area, and electrochemical surface area do not cause enough difference in the observed enhancement of OER performance. We examined the effects of microstrain on electrocatalysis, originating from lattice mismatch between different phases, using three different structural models. Specifically, we compared the Williamson—Hall method, standard stress—strain analysis, and Rietveld refinement in analyzing the structure—property relationship. Strain mapping using geometric phase analysis (GPA) further revealed significant microstrain and lattice dislocations localized near phase boundaries in the biphasic oxide, in contrast to the uniform strain in single-phase materials. The results reveal that the increased microstrain correlates well with the improved OER performance, as the biphasic oxide catalyst exhibits 2–3 times greater microstrain than Y₂Ru₂O₇ pyrochlore.

1. INTRODUCTION

The development of highly efficient water splitting technology is necessary in order to produce hydrogen, a clean energy carrier. A key challenge, however, remains in developing cost-effective and sustainable electrocatalysts that meet the demands of large-scale, industrial applications. Transition metal oxides are a major class of materials for efficiently catalyzing the oxygen evolution reaction (OER) because of their structural versatility. The catalytic properties of Mn-, Pr-, Y-, and Sr-modified, Ru-based oxides, among the OER electrocatalysts, have been studied.

While intrinsic electronic properties are important for high OER activity, recent studies suggest strain engineering can positively affect electrocatalytic performance. Strain is a measure of the deviation of atoms from their ideal lattice positions in a crystal structure. Strain often arises because of changes in bond length due to lattice mismatch and other structural factors when two different crystal structures or phases exist in a material. Thus, strain can be introduced in an electrocatalyst through the formation of solids with a mismatch

of lattice constants often accompanied by the generation of structural defects. Structural defects such as vacancies, 23,26,27 oxygen defects, 5,28,29 twinning, 30 grain boundaries, 31-33 generation of porosity, 34,35 phase and amorphous phase controls, 36-38 and heteroatom dopants 23,39-42 could be generated using different synthetic strategies. Besides uniform strain, electrocatalysts may also exhibit microstrain, which refers to localized variations in lattice spacing due to their small sizes, resulting in line broadening of Bragg peaks in the XRD pattern. This broadening arises from regional distributions of compressive and tensile strains, caused by structural inhomogeneities that can be quantified by analyzing the Bragg peak width. The introduction of controlled defects has

Received: April 25, 2025 Revised: September 21, 2025 Accepted: September 22, 2025 Published: October 5, 2025





been shown to result in an increase in the density of active sites and improved structural stability of electrocatalysts. 44,45

Catalysts experiencing strain may exhibit changes in electronic structures that include the shift in the electronic band center and overall electronic distribution, which in turn regulate the elemental steps during reactions. ^{21,46–50} The effects of strain are often explained by the postion of d-band center or an eigenstate model and subsequently used to optimize the binding energy of intermediates. ^{47,51} Strain-driven electrocatalysts have been examined for various reactions, including ethanol oxidation, ⁵² formic acid oxidation, ^{53,54} carbon dioxide reduction, ^{55,56} hydrogen evolution reaction (HER), ^{57–59} oxygen reduction reaction (ORR), ^{60–65} and OER. ^{49,66–68} However, control and proper analysis of the effect of microstrain remain challenging.

Two major approaches have been employed to introduce strain into electrocatalysts for water splitting. The first method involves the incorporation of heteroatoms into the lattice. For instance, the V cation can be introduced into CoP2 causing lattice expansion and a shift in the d-band center for enhanced OER performance.⁶⁹ Similarly, Ta in NiFe layered double hydroxide (LDH) results in lattice expansion, optimizing the electronic structure for OER activity. The second approach uses heterostructure or interface engineering to induce strain. For example, the lattice mismatch between α -MoC and MoS₂ generates strain that significantly enhances HER performance. NiTe/Ni₂P heterostructures exhibit lattice incompatibility between phosphide and telluride to induce strain, resulting in enhancement of not only OER activity but also durability through an in situ-formed protection layer.⁷² Therefore, regulating heterostructure interfaces via strain engineering presents a promising strategy for the design of high-performance OER electrocatalysts.

Herein, we hypothesize that biphasic complex oxides could optimize the electronic structure, surface, and interface properties, resulting in controlled defects. In this study, we present the synthesis of pyrochlore—perovskite biphasic oxide electrocatalyst YPrSrRuMnO $_x$ and a quantitative analysis of the lattice microstrain in heterogeneous complex oxides. Our results show that this multielement electrocatalyst exhibits the synergistic effects of combining pyrochlore-type Y–Ru oxide $(Y_2Ru_2O_7)$ and mixed perovskite-type Pr–Mn–Sr oxide $((Pr_{0.7}Sr_{0.3})MnO_3)$ on the OER electrocatalytic properties, which are superior to those of the individual phases in both activity and stability. 66,67

The enhanced OER performance of the biphasic oxide catalyst can be correlated to the introduction of lattice microstrain into the crystal structures. To quantify the strain—activity relationship, we first used Williamson—Hall (WH) analysis to quantify microstrain, in which Bragg peak broadening contributed from microstrain is differentiated from the crystallite size based on their dependency on the scattering vector. To address these limitations of the WH method such as sensitivity to instrumental broadening, we also use size—strain analysis and Rietveld refinement in our analysis to account for the effect of instrumental broadening using external standards. These two methods complement WH analysis, providing a more comprehensive and reliable assessment of microstrain.

2. EXPERIMENTAL SECTION

2.1. Synthesis. The biphasic YPrSrRuMnO $_x$ electrocatalyst was synthesized using a sol-gel method. Specifically, predetermined,

stoichiometric amounts of Y(NO₃)₃·6H₂O, Pr(NO₃)₃·6H₂O, Sr- $(NO_3)_2$, Mn·4H₂O, and Ru(NO) $(NO_3)_x(OH)_y$ were mixed with 10 mL of deionized (DI) water in a 50 mL beaker while being stirred, followed by the addition of citric acid (4 mmol, 0.8406 g). The beaker was first placed in a homemade aluminum heating block at 80 °C and left overnight to allow water to evaporate. It was then placed in a vacuum oven (VWR Symphony, approximately 10 mmHg) at 80 °C for an additional 3-4 h to remove the remaining water. Afterward, the resultant solid was crushed into a powder by using a mortar and pestle, placed in a ceramic boat, and transferred to a tube furnace (TF55035A-1, Lindberg/Blue M). The sample was then heated to 600 °C at a rate of 5 °C/min and held at this temperature for 6 h. After this heat treatment, the sample was cooled to room temperature and ground into a fine powder. This powder was placed in a ceramic boat and transferred to a tube furnace, heated to 1000 °C at a rate of 5 °C/min, and kept at this temperature for 12 h.

2.2. Material Characterization. Powder X-ray diffraction (PXRD) patterns were measured using a Rigaku Miniflex 600 diffractometer with a Cu K α X-ray source ($\lambda = 1.54056$ Å) at a scan rate of $0.01^{\circ} \ 2\theta/s$ or a Bruker D8 Advance system with a panoramic Soller slit and Cu Klpha radiation at a step size of 0.01 $^{\circ}$ 2heta and a hold time of 0.1 s/step. Scanning electron microscopy (SEM) images were obtained by using a Hitachi S4700 microscope at an acceleration voltage of 10 kV. SEM specimen was prepared by depositing catalyst powders on carbon tape on top of an SEM stub. Transmission electron microscopy (TEM) micrographs were obtained using a JEOL 2100 Cryo TEM instrument with a LaB₆ emitter at 200 kV. Scanning transmission electron microscopy (STEM)-energy dispersive X-ray spectroscopy (EDS) images were collected using a ThermoFisher Scientific Talos F200X G2 instrument. The powder sample was added to ethanol in a vial and sonicated for 30 min for dispersion. Then, 10 μL of the sample was placed on a copper grid, which was used to obtain TEM and STEM/EDS images. Energy dispersive X-ray fluorescence (XRF) was recorded on a Shimadzu EDX-700 spectrometer with a Rh X-ray source. X-ray photoelectron spectroscopy (XPS) analysis was performed using a Kratos Axis Supra+ photoelectron spectrometer.

In situ surface-enhanced Raman spectroscopy (SERS) measurements were obtained using a He/Ne laser (Meredith Instruments) at 632.8 nm in a glass and Kel-F spectroelectrochemical cell as described previously. Fig. 3 SERS data were obtained with a slit width of 50 μ m, giving an estimated spectral resolution of 6-7 cm⁻¹. Electrochemical potentials were applied with a CHI760E potentiostat (CH Instruments). Spectra were obtained from 60 individual 1 s acquisitions over each 60 s potential step. Three staircase voltammetry cycles were obtained with 50 mV increments from 0.8 to 1.6 V versus Ag/AgCl (saturated). The reference electrode was an Ag/AgCl (saturated) electrode, and the counter electrode was Pt wire. The working electrode for SERS measurements was a polycrystalline Au disk (d = 9mm) that was polished with silicon carbide grinding paper (MicroCut Plain P4000, Buehler) and subsequently subjected to 30 oxidationreduction cycles to roughen the electrode surface. Each cycle consisted of a sweep from -0.3 to $1.2\ V$ at $0.5\ V/s$, followed by a 1.3 s hold at 1.2 V versus Ag/AgCl and a sweep from 1.2 to −0.3 V at 0.5 V s⁻¹, followed by a 30 s hold at -0.3 V vs Ag/AgCl. After roughening, the catalyst ink was drop-cast on the roughened Au electrode. The electrolyte used in SERS measurements was a 0.1 M HClO₄ aqueous solution. Notably, SERS was essential in this measurement. No appreciable Raman signal was obtained from the drop-cast catalysts without a roughened Au electrode.

For geometric phase analysis (GPA), powdered samples were dispersed in ethanol and sonicated for 30 min to ensure a uniform suspension. Subsequently, 2 μ L of the solution was drop-cast onto carbon-coated copper TEM grids (Electron Microscopy Sciences, CF400-Cu) and allowed to dry completely under ambient conditions. Prior to imaging, the grids were plasma-cleaned to remove surface carbon residues and enhance the image contrast. High-angle annular dark field scanning transmission electron microscopy (HAADF-STEM) imaging was performed using a Thermo Fisher Scientific FEI Themis Z Advanced Probe Aberration-Corrected Analytical STEM

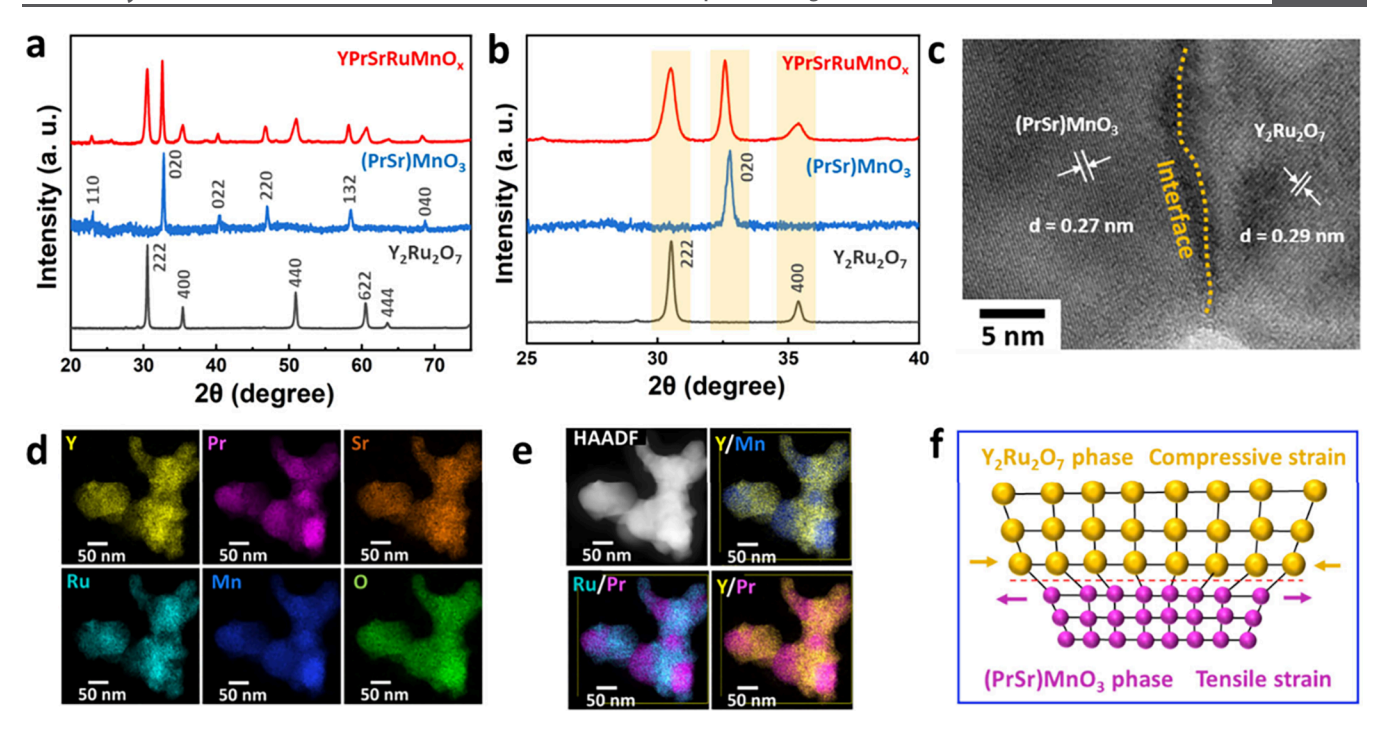


Figure 1. (a) Wide and (b) enlarged ranges of PXRD patterns, (c) TEM micrograph, (d and e) STEM-EDS elemental mapping, and (f) schematic representation of crystal strain in the YPrSrRuMnO_x catalyst made of $Y_2Ru_2O_7$ pyrochlore and $(Pr_{0.7}Sr_{0.3})MnO_3$ perovskite phases.

instrument operating at 300 kV. Images were collected with a beam current of approximately 20 pA and a semiconvergence angle of 18 mrad, using a camera length of 115 mm. To minimize drift and improve image clarity, a stack of 10-20 fast-acquisition frames (100 ns dwell time) was captured and reconstructed to produce drift-corrected high-resolution images.

2.3. Strain Analysis. *2.3.1. Williamson—Hall Method.* This method has been used for studying crystallite size and lattice strain.⁷³ It assumes that particle size and strain contribute to line broadening independently, and both follow a Cauchy-like profile. Therefore, the observed line width is the sum of the broadening due to crystallite size and lattice strain.⁷⁷ The Scherrer equation is used to determine the crystallite domain size from the broadening of X-ray diffraction peaks.⁷⁸ The equation can be expressed as

$$\beta_{\text{crystalline}} = \frac{k\lambda}{L\cos\theta} \tag{1}$$

where λ is the X-ray wavelength used, θ is the Bragg angle, L is the average crystallite size measured perpendicular to the surface of the specimen, and k is a constant and equal to 0.94 for the cubic phase crystal. The broadening due to lattice strain thus is determined by the equation

$$\beta_{\text{strain}} = 4\varepsilon \tan \theta \tag{2}$$

where ε is the strain in the material. Therefore, the total broadening can be expressed as

$$\beta_{hkl} = \frac{k\lambda}{L\cos\theta} + 4\varepsilon\tan\theta \tag{3}$$

Rearranging this equation gives

$$\beta_{hkl}\cos\theta = \frac{k\lambda}{L} + 4\varepsilon\sin\theta \tag{4}$$

A linear fit is applied to the scattered results. From this linear fit, the crystallite size is estimated from the y intercept and the strain is determined from the slope of the fit.

2.3.2. Size—Strain Plot. In this analysis, the profile of crystallite size is described by a Lorentzian function, while the strain profile is represented by a Gaussian function: 74,79

$$(d\beta \cos \theta)^2 = \frac{k}{D} (d^2\beta \cos \theta) + \left(\frac{\varepsilon}{2}\right)^2$$
 (5)

The particle size is determined from the slope of the linearly fitted data, and the root of the y intercept gives the value of strain.

2.3.3. Rietveld Refinement. This method employs a least-squares approach to refining a theoretical line profile until it closely matches the measured diffraction pattern. The principle of this method is to minimize a function M, which quantifies the difference between calculated profile $y_i^{\rm calc}$ and observed data $y_i^{\rm obs}$. The Rietveld method formulates this relationship according to the equation

$$M = \sum_{i} W_{i} \left(y_{i}^{\text{obs}} - \frac{1}{c} y_{i}^{\text{calc}} \right)^{2} \tag{6}$$

where W_i represents the statistical weight and c is an overall scale factor. By iterative variation of the parameters, the method optimizes the fit between the theoretical and experimental diffraction profiles.

In this study, Rietveld refinements were performed using TOPAS version 4.2, covering a range of 2θ from 20° to 80° . Instrumental broadening was assessed by refining a LaB₆ standard sample. The biphasic oxide structure was refined against $Y_2Ru_2O_7$ and $(Pr_{0.7}Sr_{0.3})$ -MnO₃. The refinements considered factors such as zero error, sample displacement, instrumental broadening, lattice constants, and peak broadening due to size and strain effects by using Gaussian and Lorentzian functions. Interstitial oxygen was not included in the fit.

2.3.4. Geometric Phase Analysis (GPA). GPA was used to quantitatively map the local strain distribution in the samples using the reciprocal space of HAADF-STEM images. It involves selecting specific reciprocal lattice vectors in the fast Fourier transform (FFT) of atomic-resolution images and analyzing the local phase variations associated with those vectors. These phase variations correspond to lattice displacements in real space. By applying an inverse Fourier transform to the filtered components, GPA retrieves spatially resolved phase images, from which lattice distortions and strain distributions are obtained.⁸⁰

In this study, GPA was performed by using the open-source software Strain++. Two nonparallel diffraction vectors were selected from the FFTs, and the strain component along the image x direction (ε_{xx}) was extracted to evaluate in-plane lattice distortions.

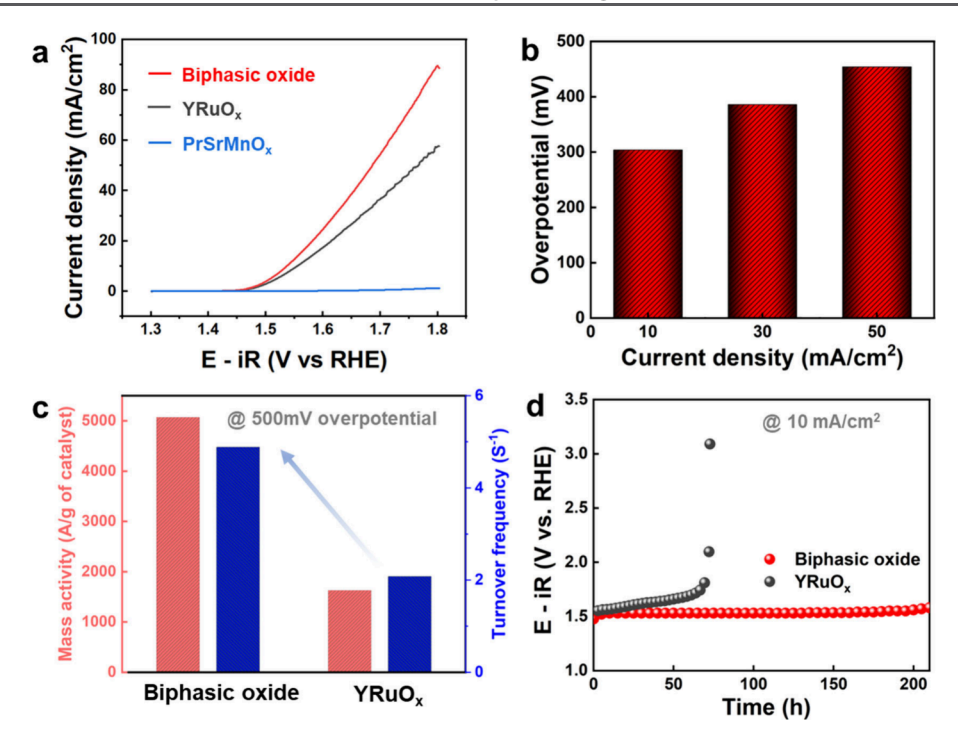


Figure 2. (a) LSV curves, (b) overpotentials for biphasic oxide at different current densities, (c) mass activity and TOF, and (d) chronopotentiometry of the biphasic YPrSrRuMnO $_x$ catalyst. Performances for single-phase Y $_2$ Ru $_2$ O $_7$ and (Pr $_{0.7}$ Sr $_{0.3}$)MnO $_3$ are included for comparison.

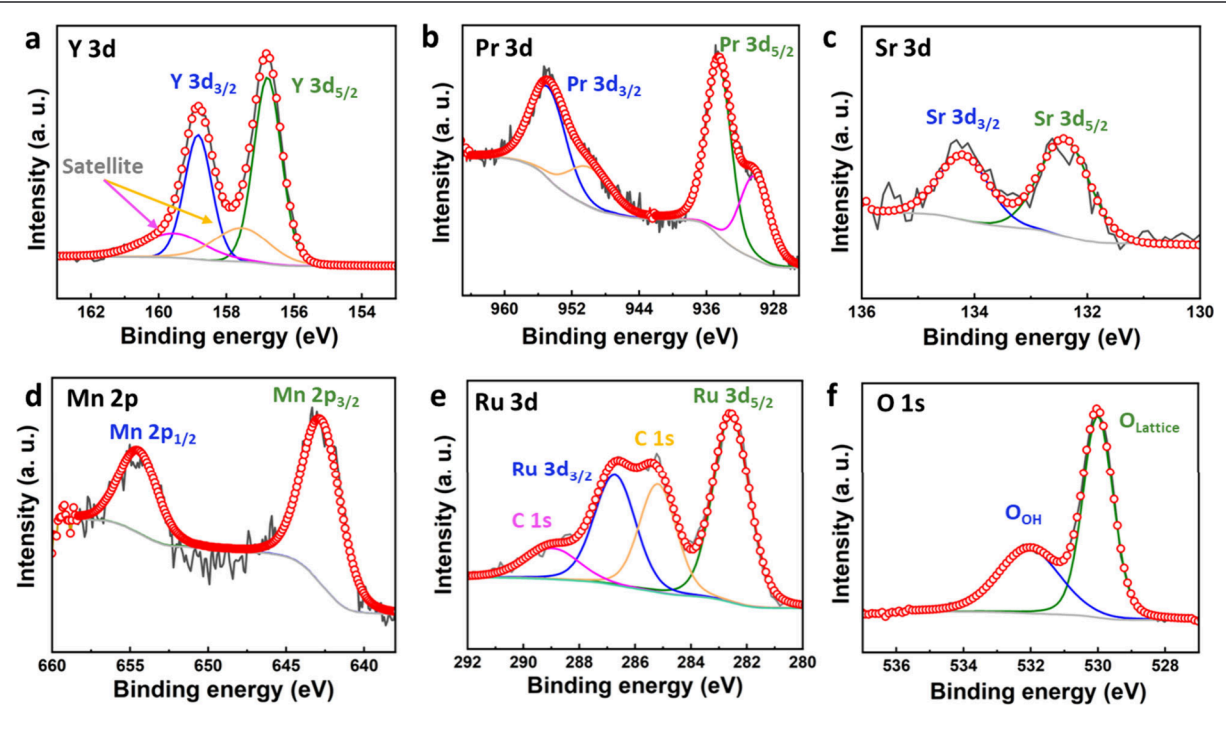


Figure 3. XPS spectra of the (a) Y 3d, (b) Pr 3d, (c) Sr 3d, (d) Mn 2p, (e) Ru 3d, and (f) O 1s regions.

2.4. Electrochemical Measurement. 2.4.1. Ink Formulation and Working Electrode Preparation. Four milligrams of catalyst powder and 4 mg of Vulcan carbon XC-72 were ground together and added to 2 mL of tetrahydrofuran (THF) and 20 μ L of a Nafion solution, and then the mixture was sonicated for 30 min in an ice bath to obtain a homogeneous mixture. One milliliter of THF and 20 mL of Nafion were mixed to obtain a blank suspension. Then, 5 μ L of the catalyst ink was drop-cast on a rotating disk electrode (RDE) and dried slowly to form a thin film working electrode. After the ink dried,

the blank was drop-cast on the RDE and dried in air to form a uniform thin film electrode.

2.4.2. Electrochemical Cell Preparation. A three-electrode cell was used to measure the electrochemical performance using a CHI 760B potentiostat (CH Instruments, Inc.). The cell is comprised of a hydrogen reference electrode (HydroFlex, Gaskatel), a platinum foil counter electrode (area of 1 cm²), and a glassy carbon working electrode (surface area of $0.196~\rm cm²$). The electrolyte used is a $0.1~\rm M$ HClO₄ aqueous solution. The electrolyte was purged with H₂ until saturation, and the reversible hydrogen electrode (RHE) was

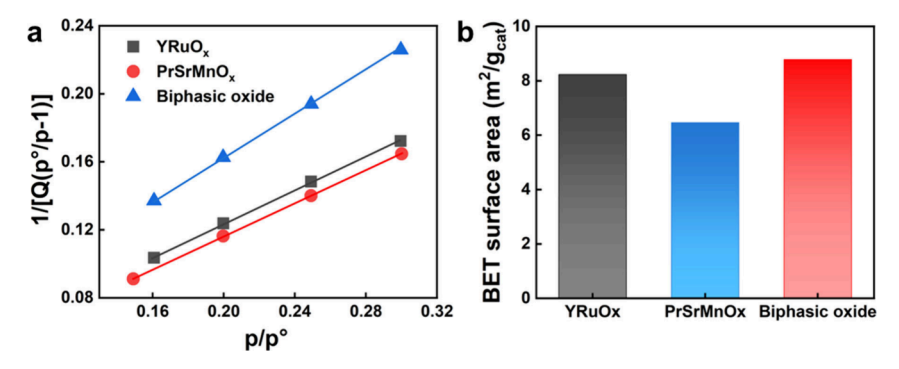


Figure 4. (a) Isotherm measurements and (b) corresponding calculated BET surface areas of the electrocatalysts presented in this study.

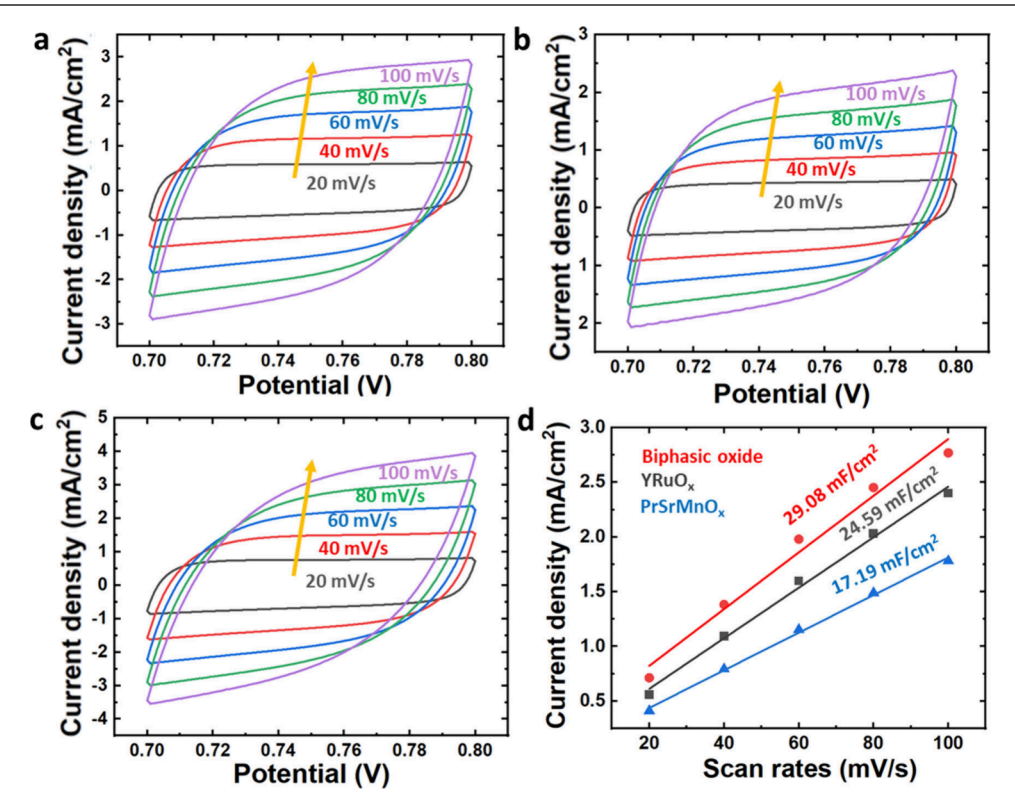


Figure 5. LSV curves of (a) $Y_2Ru_2O_7$, (b) $(Pr_{0.7}Sr_{0.3})MnO_3$, and (c) biphasic YPrSrRuMnO_x electrocatalysts in 0.1 M HClO₄ in the potential range of 0.7–0.8 V vs RHE at scan rates of 20, 40, 60, 80, and 100 mV s⁻¹. (d) Difference in current density $(\Delta j/2)$ and scan rate relationship for the biphasic YPrSrRuMnO_x, single-phase $Y_2Ru_2O_7$, and $(Pr_{0.7}Sr_{0.3})MnO_3$ electrocatalysts. The current density values were measured at 1.18 V vs RHE. The slope is equivalent to the double-layer capacitance (C_{dl}) .

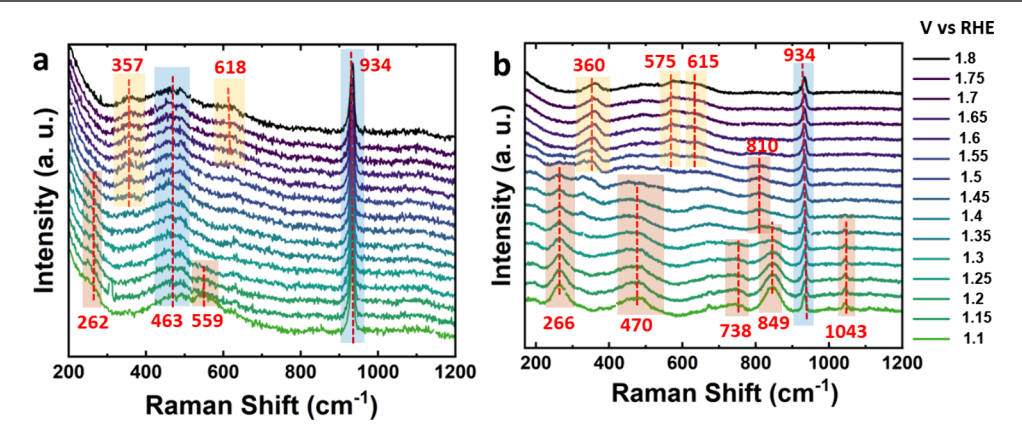


Figure 6. In situ SERS studies of (a) pyrochlore $Y_2Ru_2O_7$ and (b) pyrochlore—pervoskite biphasic YPrSrRuMnO_x electrocatalysts drop-cast on roughened Au electrodes at potentials ranging from 1.1 to 1.8 V vs RHE.

calibrated in a H_2 -saturated electrolyte solution before testing. After the calibration, the electrolyte was purged with O_2 for 30 min, and all measurements were performed under that condition.

2.4.3. Linear Sweep Voltammetry Study. Linear sweep voltammetry (LSV) was performed at a scan rate of 10 mV s⁻¹ between 1.3 and 1.8 V. The RDE rotating speed was set at 1600 rpm.

2.4.4. Chronopotentiometry Study. Chronopotentiometry (CP) measurements were obtained at a constant current density of 10 mA cm $^{-2}$ using an RHE reference electrode and FTO glass as the substrate. The FTO glass was 1 cm wide and 5 cm long, with a working area of 1 cm \times 1 cm. In a typical procedure, 400 μ L of the prepared ink was drop-cast onto the FTO using a 100 μ L pipet.

3. RESULTS AND DISCUSSION

3.1. Crystal Structure. The catalysts were prepared using the sol-gel method,⁵ which was characterized using XRD

Table 1. Assignments of SERS Peaks for Y₂Ru₂O₇ and Biphasic YPrSrRuMnO_x Oxides

peak position (cm ⁻¹)		assignment		
$Y_2Ru_2O_7$	$YPrSrRuMnO_x$	Ru	Y-based pyrochlore	Y ₂ Ru ₂ O ₇
262	266	Ru-O ^{85,86}	octahedral deformation and cation displacement ⁸⁷	
357	360	Ru-O ⁸⁵	octahedral deformation and cation displacement ⁸⁷	F_{2g}^{89}
463	470	RuO ₂ ^{85,86,90}	octahedral bend ⁸⁷	
559	575	RuO_2^{90}	F_{2g}^{91}	F_{2g}^{89}
618	615		F_{2g}^{91}	
	738		MO ₆ stretch ⁸⁷	
	810	RuO ₄ 86,90	MO ₆ stretch ⁸⁷	
	849	RuO ₄ 90,92	MO ₆ stretch ⁸⁷	

between 20° and 80° 2 θ . Figure 1a shows the PXRD pattern of the YPrSrRuMnO $_x$ biphasic oxide, revealing the coexistence of two distinct phases. One phase contains Y–Ru–O, while the other phase contains Sr–Pr–Mn–O. Y–Ru–O (phase 1) resembles cubic-type pyrochlore of Y₂Ru₂O₇ (JCPDS# 01-083-0637), whereas Sr–Pr–Mn–O (phase 2) can be assigned to the orthorhombic perovskite of (Pr_{0.7}Sr_{0.3})MnO₃ (JCPDS# 01-081-0820). Rietveld refinement analysis indicates that biphasic oxide is composed of approximately 54.35% phase 1 and 45.65% phase 2, underscoring the slight dominance of the Y–Ru–O phase in the sample.

Figure 1b presents the XRD pattern at 2θ values between 25° and 40° to investigate the peak shift and broadening. While the peak shift is typically indicative of lattice strain, no significant changes in peak positions are observed. Instead, noticeable peak broadening is detected, which may be attributed to microstrain. Since two distinct phases exist, the crystallite size and d spacing are expected to be different. Thus, the line broadening may arise from both compressive and tensile strained regions, induced by the coexistence of two distinct phases. Specifically, the peaks corresponding to the (222) and (400) planes of the $Y_2Ru_2O_7$ pyrochlore phase and the (020) plane of the $Y_2Ru_2O_7$ phase perovskite phase remain unchanged in position but display significant broadening, indicative of the presence of microstrain.

Transmission electron microscopy was performed to study the structural details of the two phases (Figure 1c). An interface boundary was clearly observed at the heterojunction between the Y₂Ru₂O₇ and (Pr_{0.7}Sr_{0.3})MnO₃ phases (yellow dotted line). Figure S1 provides information on the d spacing measurements of these two phases, measured by TEM. Specifically, a d spacing of 0.29 nm was observed for the (222) plane of the Y₂Ru₂O₇ pyrochlore phase, while a d spacing of 0.27 nm could be attributed to the (020) plane of the (Pr_{0.7}Sr_{0.3})MnO₃ perovskite phase, highlighting the differences in interplanar spacing between the two. The observed differences in d spacing are from the distinct crystallographic features, which should result in varied geometric and electronic environments. STEM-EDS images indicate that Y, Pr, Sr, Ru, Mn, and O are distributed across the particle, and the unevenness, in contrast, suggests phase separation exists, agreeing well with the XRD data. Noticeably, elemental distributions of Y and Ru overlap (in Y-Ru-O), while Pr, Sr, and Mn show a similar elemental distribution in the particle (Pr-Sr-Mn-O). This observation indicates that Y and Ru exist in a separate phase from Mn, Pr, and Sr, further confirming the phase separation across the sample. The overlaid images of Y/Mn, Ru/Pr, and Y/Pr show the boundary between the two phases in a heterostructure (Figure 1e). SEM-EDS mapping shows that both phases are homogeneously distributed throughout the sample (Figure S2).

The lattice mismatch observed at the phase boundaries, as illustrated in Figure 1f, is a common feature of this biphasic structure. Strain is generated at the interface between the larger crystal structure of the Y-Ru-O phase, characterized by its *d* spacing of 0.29 nm, and the Pr-Sr-Mn-O phase, with a *d* spacing of 0.27 nm. This lattice mismatch is significant, since induced strain can lead to the formation of defects and distortions within the crystal lattice. The presence of high-level defects often results in enhanced catalytic activity, as these defects provide cues for activating the sites that control the catalytic steps on the surface.

3.2. Characterization of Catalytic Performance in **Oxygen Evolution Reaction.** Linear sweep voltammetry was conducted utilizing a three-electrode setup in a 0.1 M HClO₄ aqueous solution. Figure 2a illustrates that the pyrochloreperovskite biphasic oxide exhibits a current density that is higher than those of the two individual phases at the same potential (100% iR correction). While the Y-Ru-Ocontaining phase demonstrates OER activity, the Pr-Sr-Mn-O-containing phase does not exhibit any increment in current density with an increase in potential. This observation suggests that although the Pr-Ru-Mn-O phase lacks OER activity, its presence contributes to the overall activity of the biphasic catalyst. Figure 2b shows that the overpotential for the biphasic oxide catalyst is 304 mV at a current density of 10 mA cm⁻², 386 mV at 30 mA cm⁻², and 454 mV at 50 mA cm⁻². The biphasic oxide catalyst has 3.11 times the mass activity and 2.35 times the turnover frequency (TOF) of single-phase $Y_2Ru_2O_7$ (Figure 2c). Compared to commercial RuO₂, the biphasic oxide catalyst exhibited 13 times greater mass activity and 36 times higher TOF (Figure S3). The physically mixed Y₂Ru₂O₇/PrSrMnO_x sample, with an identical overall composition, showed lower OER activity than Y2Ru2O7, confirming the inactivity and the diluting effect of the PrSrMnO_r electrocatalyst (Figure S4). A comparison of Sr-, Mn-, and Pr-doped Y₂Ru₂O₇ electrocatalysts revealed their activity is lower than that of undoped YRuO_x (Figure S5). These results rule out mixing and doping as the main origin of the observed OER enhancement, further signifying that the improved performance of the biphasic oxide arises from other

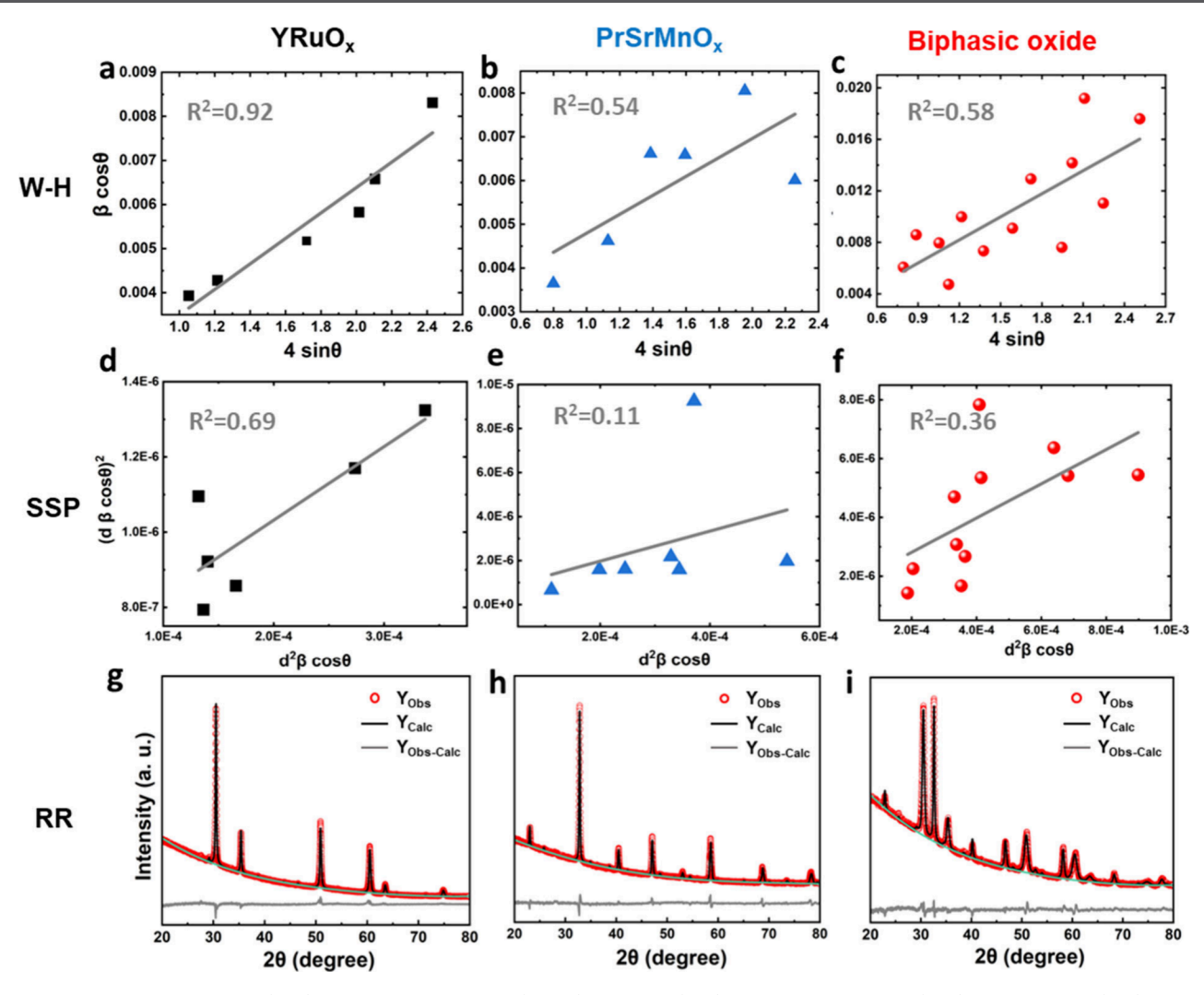


Figure 7. Strain analysis using (a-c) the Williamson-Hall (W-H) method, (d-f) the size-strain plot (SSP) method, and (g-i) Rietveld refinement (RR) for the (a, d, and g) single-phase $Y_2Ru_2O_7$, (b, e, and h) $(Pr_{0.7}Sr_{0.3})MnO_3$ and (c, f, and i) biphasic YPrSrRuMnO_x electrocatalysts.

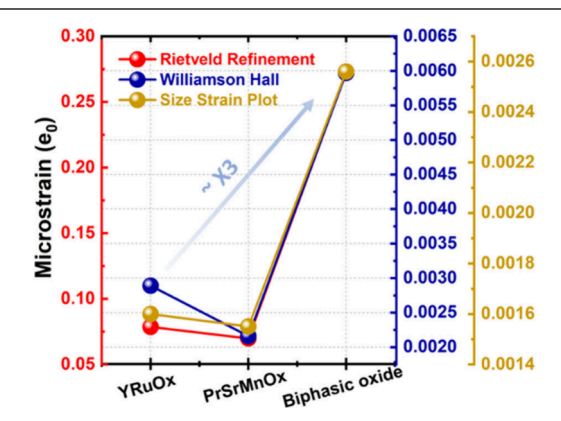


Figure 8. Comparison of microstrains obtained by using the three different analytical methods.

structural cues, such as interface-induced effects. Chronopotentiometry studies show that biphasic oxide is stable for more than 200 h in 0.1 M HClO₄ without considerable degradation at a current density of 10 mA cm⁻², whereas the $Y_2Ru_2O_7$ phase degrades in about 70 h (Figure 2d).

3.3. Study of the Effects of Catalyst Structure on OER Activity. *3.3.1. X-ray Photoelectron Spectroscopy.* X-ray

photoelectron spectroscopy was performed to determine the oxidation state of cationic species on the surface of Y₂Ru₂O₇ and biphasic YPrSrRuMnOx electrocatalysts. The XPS survey confirms the presence of Y and Ru with no detectable impurities in Y₂Ru₂O₇, implying that the sample is highly pure (Figure S6). Similarly, Y, Pr, Sr, Ru, and Mn are all detected on the surface of the biphasic YPrSrRuMnOx electrocatalyst (Figure S7). The peaks at 156.8 and 158.8 eV are assigned to Y $3d_{5/2}$ and Y $3d_{3/2}$, respectively, which correspond to the Y³⁺ oxidation state (Figure 3a).5 Two satellite peaks are observed at 159.6 and 157.5 eV, further confirming the oxidation state of Y. Similarly, the Y 3d peaks of Y₂Ru₂O₇ suggest that the oxidation state of this cation is 3+ in Figure S8a. XPS data indicate that Pr3+ primarily exhibits an asymmetric peak for $3d_{5/2}$ at 934.5 eV, with a spin-orbit splitting of 20.3 eV to $3d_{3/2}$ at 954.8 eV (Figure 3b). 81,82 The weak satellite peaks at lower binding energies of 930.3 and 949.9 eV are from the screened 3d94f².81 The XPS data show the peaks at 132.4 and 134.2 eV, which are assigned to Sr $3d_{5/2}$ and Sr $3d_{3/2}$, respectively, and correspond to Sr²⁺ (Figure 3c),⁸³ and Mn 2p peaks at 642.8 and 654.7 eV with a satellite peak at 645.9 eV corresponding to 2p_{3/2} are assigned to Mn³⁺ (Figure 3d).⁸⁴ XPS data cannot readily be used to quantify the valence of Ru properly due to the overlaps between Ru 3d and C 1s regions

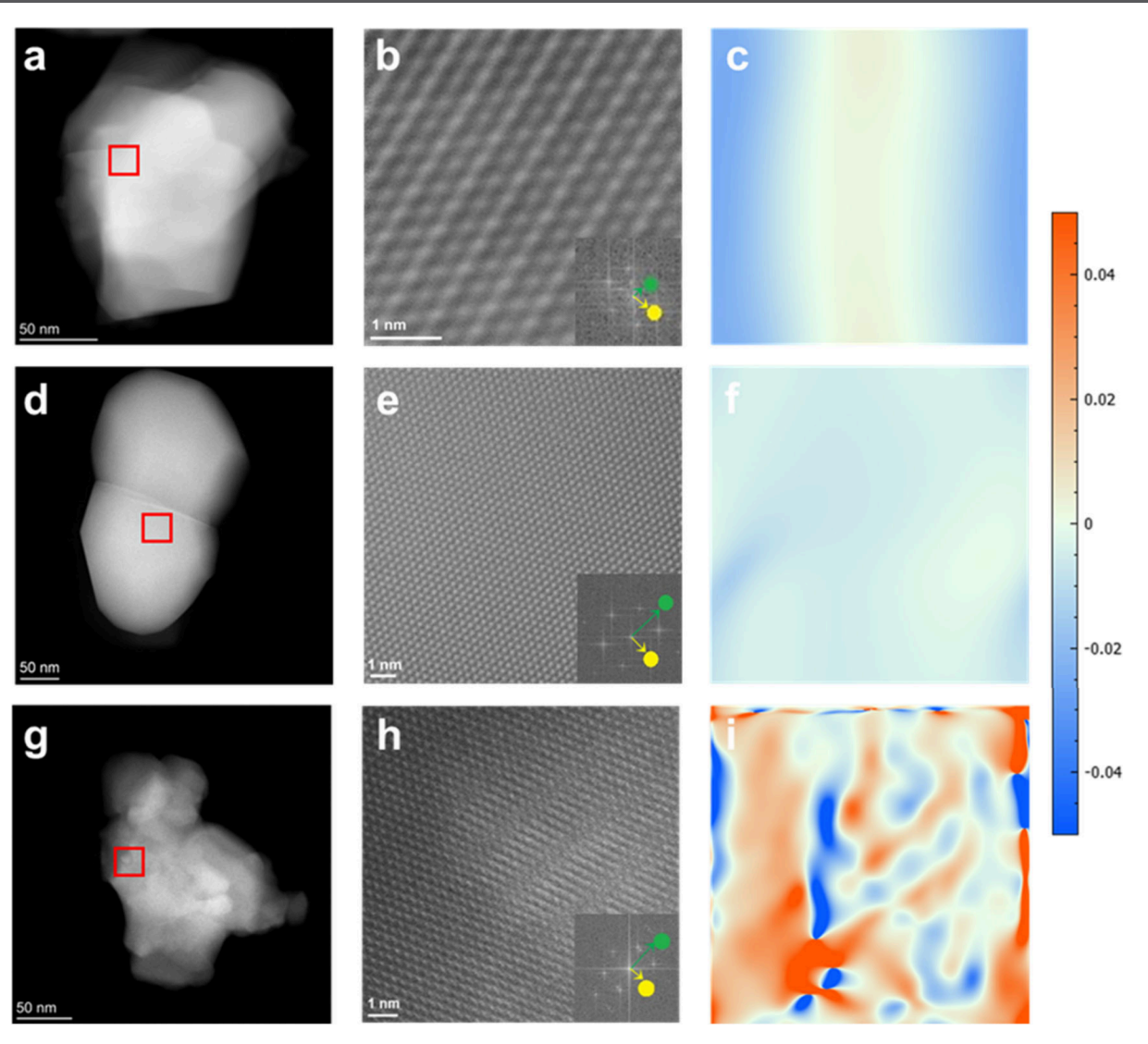


Figure 9. HAADF-STEM images and strain component maps of (a-c) $Y_2Ru_2O_7$, (d-f) $(Pr_{0.7}Sr_{0.3})MnO_3$, and (g-i) biphasic YPrSrRuMnO_x oxides. The red boxes in low-magnification images (a, d, and g) indicate regions selected for high-resolution STEM imaging shown in panels b, e, and h, respectively, with insets displaying the corresponding FFT patterns. In each FFT inset, yellow and green arrows point to the reciprocal lattice vectors used for GPA along the x and y directions, respectively, corresponding to the yellow and green circles. Panels c-i show the ε_{xx} strain component maps derived from GPA for each sample, where tensile strain is represented by red and compressive strain by blue.

as the activated carbon support was used as the support. The peaks were deconvoluted carefully; peaks at 285.2 and 289 eV are assigned to C 1s, and the peaks at 282.6 eV for 3d_{5/2} and 286.7 eV for $3d_{3/2}$ Ru are present, indicating the oxidation is dominated by the 4+ state (Figure 3e). Similarly, XPS analysis of the Ru 3d peaks of Y₂Ru₂O₇ suggests that Ru exists in the 4+ oxidation state, as well (Figure S8b). The XPS study of O 1s spectra of biphasic oxide could be fitted to two species, namely, the lattice oxygen (O_{Lattice}) at 530.0 eV and the hydroxyl group (OOH) at 532 eV (Figure 3f), which match quite well with Y₂Ru₂O₇ (Figure S8c).³⁸ The XPS study of Ru 3p spectra shows that there is no detectable difference in the Ru^{4+} peaks at 464.4 eV $(3p_{3/2})$ and 486.7 eV $(3p_{1/2})$ between Y₂Ru₂O₇ and YPrSrRuMnO_x electrocatalysts (Figure S9). The XPS characterization suggests that the biphasic oxide catalyst retains the same or similar oxidation states as those found in Y₂Ru₂O₇. This homogeneity across the oxidation states leads to the conclusion that a change in oxidation state should not be a contributing factor to the enhancement of OER performance,

indicating that other structural properties need to be explored for the observed difference in catalytic efficiency.

3.3.2. BET and ECSA Analyses. Besides analyzing the surface structures, we also examined the specific surface area and the electrochemical active surface area. Figure 4a presents the nitrogen adsorption isotherm data, plotted according to the Brunauer-Emmett-Teller (BET) analysis in the relative pressure range of 0.14-0.30. Linear fitting of the BET plots yielded the slope and intercept used to calculate the values of the monolayer adsorption and the corresponding specific surface area. Among the three catalysts, PrSrMnO_x exhibited the steepest slope, corresponding to the lowest monolayer adsorption capacity and, thus, the smallest specific surface area. The biphasic oxide (YPrSrRuMnO_x) and YRuO_x exhibited similar slopes in the BET plot, indicating comparable adsorption capacities, though the biphasic oxide showed a slightly higher intercept, leading to a marginally greater surface area. The BET surface areas were determined to be 8.67 m² g⁻¹ for YPrSrRuMnO_x, 8.23 m² g⁻¹ for Y₂Ru₂O₇, and 6.46 m² g⁻¹ for (Pr_{0.7}Sr_{0.3})MnO₃ (Figure 4b). The values of BET specific

surface areas for all three solids are within the typical range for solid phase OER electrocatalysts of this kind without major porosity. Thus, it appears that the observed difference in OER activity cannot be directly correlated to the specific surface

We further studied the electrochemically active surface area (ECSA) by analyzing the differences in current density $(\Delta j/2)$ as a function of scan rate (Figure 5a-c), which were obtained from the LSV curves of the electrocatalysts in the non-Faradaic region. In this analysis, the slope gives the double-layer capacitance $(C_{\rm dl})$ shown in Figure 5d, which is proportional to the active surface area. The results suggest that the biphasic oxide electrocatalyst has a slightly larger active surface area than do the two parent phases. We note that while the biphasic YPrSrMnO_x catalyst exhibits more than 3 times the mass activity of single-phase $Y_2Ru_2O_7$, its $C_{\rm dl}$ value is only 29.08/24.59 = 1.18 times of that for $Y_2Ru_2O_7$. Thus, other factors could further contribute to the enhancement in OER activity.

3.3.3. In Situ Surface-Enhanced Raman Spectroscopy (SERS). We performed a comparative in situ SERS study between pyrochlore $Y_2Ru_2O_7$ and pyrochlore—perovskite

(SERS). We performed a comparative in situ SERS study between pyrochlore Y₂Ru₂O₇ and pyrochlore-perovskite biphasic YPrSrRuMnO_x electrocatalysts. Figure 6a shows SERS spectra obtained from Y₂Ru₂O₇ drop-cast on a roughened gold electrode at potentials ranging from 0.9 to 1.6 V versus Ag/AgCl (saturated). Assignments of characteristic Raman peaks are summarized in Table 1. Notably, the intensity of the SERS peak at 262 cm⁻¹ decreased as the applied potential increased. This peak is attributed to either the Ru-O vibration mode from Ru at the surface or octahedral deformations coupled with cation displacements of pyrochlore. 85-87 Two peaks, one at 357 cm⁻¹ and the other at 618 cm⁻¹, appeared at potentials above the onset of the OER and were attributed to a Ru-O vibration from Ru at the surface or octahedral deformations coupled with cation displacements of the pyrochlore and the F_{2g} mode of pyrochlore, respectively. These two modes were only observed at potentials when the OER occurred. The peak observed at 463 cm⁻¹ maintained the same intensity throughout the potentials and was assigned to the bending mode octahedral site in pyrochlore.⁸⁷ The peak at 934 cm⁻¹ is from perchlorate species in the electrolyte.⁸⁸ The changes in peak intensity shown here are reversible during the reverse scan, as shown in Figure S10. Bulk Raman data are in good agreement with the Raman spectroscopy results for bulk Y₂Ru₂O₇ reported previously (Figure S11).

Figure 6b shows the SERS spectra obtained from the pyrochlore-perovskite biphasic YPrSrRuMnO_x catalyst dropcast on a roughened gold electrode at potentials ranging from 1.1 to 1.8 V versus RHE. Three additional SERS peaks were observed at 738, 810, and 849 cm⁻¹. The intensity of all of these peaks decreased as potential was applied and disappeared once the onset potentials of the OER were reached. These peaks are therefore not representative of the surface during the OER, suggesting that they are not involved in or are not the slow step in the OER mechanism. The peaks present at the potentials where OER occurs are the 360, 470, and 615 cm⁻¹ vibrational modes, the same vibrational modes seen at OER potentials as for Y₂Ru₂O₇. The changes in peak intensity observed here are reversible, as demonstrated during the cathodic scan in Figure S12. Peak shifts and the broadness of these peaks likely occurred due to surface strain, which changes the bond lengths and therefore vibrational energies. We note that the peak centered at 470 cm⁻¹ decreases in intensity at the more positive potentials but does not decrease to zero. The

presence of the same peaks at potentials where the OER occurs for both pyrochlore and biphasic pyrochlore—perovskite catalysts indicates a similar change in surface structure during the OER, suggesting similar active sites for the oxygen evolution reaction in these two catalyst systems.

3.3.4. Microstrain Analysis. We examined the microstrain, also known as the local lattice strain, in these electrocatalysts. Microstrain is a measure of the local atomic deviation from their ideal positions within a lattice structure.³² This deviation can be analyzed based on the broadening of XRD peaks. Microstrain thus is commonly used to assess structural disorders caused by various defects, such as stacking fault, twin, grain boundary, and dislocation. 32,93-95 Based on X-ray diffraction data, we carried out microstrain analysis using the Williamson-Hall method, size-strain relationship, and Rietveld refinement. The Williamson-Hall method, which assumes that strain is uniform in all crystallographic directions, is best suited for studying isotropic solid materials, where properties are often independent of the measurement direction. In this work, the term β cos θ is plotted against 4 $\sin \theta$ for the preferred orientations of $Y_2Ru_2O_7$ (Figure 7a), $(Pr_{0.7}Sr_{0.3})MnO_3$ (Figure 7b), and biphasic oxide (Figure 7c). In this plot, the slope of the fitted line corresponds to the strain while the y intercept represents the particle size. The results depicted in these Williamson-Hall plots indicate that the line broadening was essentially isotropic, suggesting that the domains are largely isotropic and that there is also a contribution from microstrain. Since the solids have isotropic line broadening, the size-strain plot (SSP) is considered a more accurate evaluation of size and strain parameters. ⁷⁴ This approach is advantageous because it places less emphasis on data from diffractions at large angles, where the precision is typically lower. Similar to the Williamson-Hall method, the term $(d\beta \cos \theta)^2$ is plotted against $(d^2\beta \cos \theta)$ for all orientations of Y₂Ru₂O₇, (Pr_{0.7}Sr_{0.3})MnO₃, and biphasic oxides (Figure 7d-f). In this approach, the particle size is determined from the slope of the linearly fitted data, while the square root of the y intercept gives the strain. Tables S1 and S2 summarize the calculated values of strain using the Williamson-Hall method and size-strain plot method, respectively.

Rietveld refinement was further used in the microstrain analysis (Figure 7g-i). This third method provides additional structural information, such as the lattice parameter, atomic position, and thermal vibration. As it uses the full diffraction pattern, Rietveld refinement is suited for analyzing complex structures with overlapping peaks. In this work, we used the TOPAS software to perform refinement with the grain size in the range of 50–150 nm as determined by SEM (Figure S13). The refinement results, summarized in Table S3, show low R factors ($R_{\rm exp}$, $R_{\rm wp}$, and $R_{\rm p}$) and goodness-of-fit (GOF) values close to 1, indicating a high-quality fit between the experimental and calculated patterns. In the biphasic YPrSrRuMnO_r electrocatalyst, the two phases exhibit different degrees of microstrain, and the weighted average values are used to estimate the microstrain in the oxide solid (Figure S14). Interestingly, the biphasic oxide of YPrSrRuMnO_x shows the highest degree of microstrain among the three, and the value is 2-3 times larger than that of its single-phase solids (Figure 8). Thus, this difference in microstrain may likely be attributed to the observed higher OER activity for the biphasic oxide of YPrSrRuMnOx when compared with that of singlephase Y₂Ru₂O₇. These results also suggest that the Rietveld refinement offers more reliable strain measurements by

considering the full diffraction pattern and allowing complex modeling of anisotropic structural features, which should also be the best analytical method for analyzing the strain effect.

The strain distribution was analyzed using GPA on atomicresolution HAADF-STEM images in the samples of Y2Ru2O7 (Figure 9a-c), (Pr_{0.7}Sr_{0.3})MnO₃ (Figure 9d-f), and biphasic YPrSrRuMnO_x (Figure 9g-i) electrocatalysts. The ε_{xx} strain maps highlight the tensile and compressive regions, with red indicating tensile strain and blue representing compressive strain (Figure 9c,f,i). In the biphasic YPrSrRuMnO_x sample, the abrupt color variations indicate significant lattice dislocations near the interfacial regions, suggesting the presence of microstrain arising from phase boundaries or lattice mismatch. This is further supported by elemental EDS mapping, which reveals compositional heterogeneity at the interface in the same particle (Figure S15). In contrast, the strain maps of single-phase oxides Y₂Ru₂O₇ and (Pr_{0.7}Sr_{0.3})-MnO₃ exhibit relatively uniform strain distributions with minimal lattice dislocations. These findings are consistent with the XRD results, which showed broader peaks and higher microstrain values in the biphasic oxide than in the singlephase materials.

It appears that the enhancement in the OER through the creation of a biphasic solid oxide can be a general phenomenon in complex oxides. We synthesized additional biphasic electrocatalysts YPrSrRuMnVO_x and YPrSrRuMnTiO_x, each comprising Y₂Ru₂O₇ as one phase and PrVO₄ or SrTiO₃ as the other phase. Notably, although PrVO₄ or SrTiO₃ alone displays minimal intrinsic OER activity, their corresponding biphasic oxides exhibited significantly enhanced performance relative to their single phases (Figure S16). These results suggest that phase interactions and microstrain effects at the interface can result in a superior OER activity in complex oxides.

4. CONCLUSION

Our study highlights the effectiveness of lattice-strain engineering in enhancing the oxygen evolution reaction performance of biphasic YPrSrRuMnO_x oxide catalysts. The biphasic structure, consisting of pyrochlore-structured Y₂Ru₂O₇ and perovskite-structured (Pr_{0.7}Sr_{0.3})MnO_x, shows significantly improved catalytic activity and stability compared to single-phase Y2Ru2O7. Our analysis revealed that the microstrain of the biphasic oxide is 2-3 orders of magnitude higher than that of the single-phase solids due to lattice mismatch, which plays a crucial role in this enhancement of the OER activity. The data from strain-OER property analysis indicate that Rietveld refinement offers the most appropriate correlation, indicating the need to consider anisotropic structural features in the strain measurements. This work demonstrates the potential of lattice-strain engineering as a strategy for designing high-performance catalysts and lays the groundwork for the further exploration of biphasic electrocatalysts.

ASSOCIATED CONTENT

Supporting Information

The Supporting Information is available free of charge at https://pubs.acs.org/doi/10.1021/acs.chemmater.5c01004.

Chemicals used; mass activity and turnover frequency calculation; figures showing TEM data analysis, EDS, additional CVs, XPS data, Raman spectroscopy data,

SEM images, and HAADF-STEM image; and tables providing parameters on the Williamson-Hall method, size-strain analysis, and Rietveld refinement method (PDF)

AUTHOR INFORMATION

Corresponding Author

Hong Yang — Department of Chemical and Biomolecular Engineering, University of Illinois Urbana-Champaign, Urbana, Illinois 61801, United States; Department of Chemistry, University of Illinois Urbana-Champaign, Urbana, Illinois 61801, United States; Materials Research Laboratory, The Grainger College of Engineering, University of Illinois Urbana-Champaign, Urbana, Illinois 61801, United States; orcid.org/0000-0003-3459-4516; Email: hy66@illinois.edu

Authors

Bidipta Ghosh – Department of Chemical and Biomolecular Engineering, University of Illinois Urbana-Champaign, Urbana, Illinois 61801, United States

Gavin S. Lindsay – Department of Chemistry, University of Illinois Urbana-Champaign, Urbana, Illinois 61801, United States

Sohini Mandal — Department of Chemistry, University of Illinois Urbana-Champaign, Urbana, Illinois 61801, United States

Toby Woods — Center of Research and Educational Support, X-ray Diffraction Laboratory, School of Chemical Sciences, University of Illinois Urbana-Champaign, Urbana, Illinois 61801, United States; orcid.org/0000-0002-1737-811X

Qian Chen — Department of Chemical and Biomolecular Engineering, University of Illinois Urbana-Champaign, Urbana, Illinois 61801, United States; Department of Chemistry, University of Illinois Urbana-Champaign, Urbana, Illinois 61801, United States; Department of Materials Science and Engineering, University of Illinois Urbana-Champaign, Urbana, Illinois 61801, United States; Materials Research Laboratory, The Grainger College of Engineering, University of Illinois Urbana-Champaign, Urbana, Illinois 61801, United States; orcid.org/0000-0002-1968-441X

Andrew A. Gewirth — Department of Chemistry, University of Illinois Urbana-Champaign, Urbana, Illinois 61801, United States; orcid.org/0000-0003-4400-9907

Complete contact information is available at: https://pubs.acs.org/10.1021/acs.chemmater.5c01004

Notes

The authors declare no competing financial interest.

ACKNOWLEDGMENTS

This work was supported by the U.S. National Science Foundation (NSF CBET-2055734) and the U.S. Department of Energy, Office of Science, Science Foundations for Energy Earthshots Program (DE-SC0024892). The authors thank Ram Gupta for the experimental help. EM characterizations were carried out at the Illinois Materials Research Laboratory Central Facilities. X-ray diffraction was carried out at the George L. Clark X-ray Facility and 3M Materials Laboratory, School of Chemical Science, at UIUC and Illinois Materials Research Laboratory Central Facilities. Any opinions, findings,

and conclusions or recommendations expressed in this publication are those of the authors and do not necessarily reflect the views of the U.S. National Science Foundation or Department of Energy.

REFERENCES

- (1) Chatenet, M.; Pollet, B. G.; Dekel, D. R.; Dionigi, F.; Deseure, J.; Millet, P.; Braatz, R. D.; Bazant, M. Z.; Eikerling, M.; Staffell, I.; et al. Water electrolysis: From textbook knowledge to the latest scientific strategies and industrial developments. *Chem. Soc. Rev.* **2022**, *51*, 4583–4762.
- (2) Song, J.; Wei, C.; Huang, Z.-F.; Liu, C.; Zeng, L.; Wang, X.; Xu, Z. J. A review on fundamentals for designing oxygen evolution electrocatalysts. *Chem. Soc. Rev.* **2020**, *49*, 2196–2214.
- (3) Buttler, A.; Spliethoff, H. Current status of water electrolysis for energy storage, grid balancing and sector coupling via power-to-gas and power-to-liquids: A review. *Renew. Sustain. Energy Rev.* **2018**, *82*, 2440–2454.
- (4) Zhang, X.; Shi, C.; Chen, B.; Kuhn, A. N.; Ma, D.; Yang, H. Progress in hydrogen production over transition metal carbide catalysts: challenges and opportunities. *Curr. Opin. Chem. Eng.* **2018**, *20*, 68–77.
- (5) Ghosh, B.; Zhang, C.; Frick, S.; Cho, E. J.; Woods, T.; Yang, Y.; Perry, N. H.; Klein, A.; Yang, H. Defect engineering in composition and valence band center of $Y_2(Y_xRu_{1-x})_2O_{7-\delta}$ pyrochlore electrocatalysts for oxygen evolution reaction. *J. Am. Chem. Soc.* **2024**, *146*, 18524–18534.
- (6) Suen, N.-T.; Hung, S.-F.; Quan, Q.; Zhang, N.; Xu, Y.-J.; Chen, H. M. Electrocatalysis for the oxygen evolution reaction: recent development and future perspectives. *Chem. Soc. Rev.* **2017**, *46*, 337–365
- (7) Wan, R.; Yuan, T.; Wang, L.; Li, B.; Liu, M.; Zhao, B. Earthabundant electrocatalysts for acidic oxygen evolution. *Nat. Catal.* **2024**, *7*, 1288–1304.
- (8) Jones, T. E.; Teschner, D.; Piccinin, S. Toward realistic models of the electrocatalytic oxygen evolution reaction. *Chem. Rev.* **2024**, 124, 9136–9223.
- (9) Zhao, J.-W.; Li, Y.; Luan, D.; Lou, X. W. Structural evolution and catalytic mechanisms of perovskite oxides in electrocatalysis. *Sci. Adv.* **2024**, *10*, No. eadq4696.
- (10) Zhao, J. W.; Yue, K.; Wu, L.; Yang, J.; Luan, D.; Zhang, X.; Lou, X. W. Surface transformation in lanthanum nickelate for enhanced oxygen evolution catalysis. *Angew. Chem., Int. Ed.* **2025**, *64*, No. e202507144.
- (11) Zhao, Z.-J.; Liu, S.; Zha, S.; Cheng, D.; Studt, F.; Henkelman, G.; Gong, J. Theory-guided design of catalytic materials using scaling relationships and reactivity descriptors. *Nat. Rev. Mater.* **2019**, *4*, 792–804
- (12) Sun, H. A.; Xu, X. M.; Kim, H.; Jung, W.; Zhou, W.; Shao, Z. P. Electrochemical water splitting: Bridging the gaps between fundamental research and industrial applications. *Energy Environ. Mater.* **2023**, *6*, No. e12441.
- (13) Zeng, S.-P.; Shi, H.; Dai, T.-Y.; Liu, Y.; Wen, Z.; Han, G.-F.; Wang, T.-H.; Zhang, W.; Lang, X.-Y.; Zheng, W.-T.; Jiang, Q. Lamella-heterostructured nanoporous bimetallic iron-cobalt alloy/oxyhydroxide and cerium oxynitride electrodes as stable catalysts for oxygen evolution. *Nat. Commun.* 2023, 14, 1811.
- (14) Vazhayil, A.; Vazhayal, L.; Thomas, J.; Ashok C, S.; Thomas, N. A comprehensive review on the recent developments in transition metal-based electrocatalysts for oxygen evolution reaction. *Appl. Surf. Sci. Adv.* **2021**, *6*, 100184.
- (15) Fabbri, E.; Schmidt, T. J. Oxygen evolution reaction—The enigma in water electrolysis. ACS Catal. 2018, 8, 9765–9774.
- (16) Han, N.; Feng, S.; Liang, Y.; Wang, J.; Zhang, W.; Guo, X.; Ma, Q.; Liu, Q.; Guo, W.; Zhou, Z.; et al. Achieving efficient electrocatalytic oxygen evolution in acidic media on yttrium ruthenate pyrochlore through cobalt incorporation. *Adv. Funct. Mater.* **2023**, 33, 2208399.

- (17) Liu, T.; Guo, H.; Zhang, Q.; Fujishige, M.; Endo, M.; Zhang, Z.; Wang, F. Insulator-transition-induced degradation of pyrochlore ruthenates in electrocatalytic oxygen evolution and stabilization through doping. *Angew. Chem., Int. Ed.* **2024**, *63*, No. e202412139.
- (18) Feng, Z.; Dai, C.; Zhang, Z.; Lei, X.; Mu, W.; Guo, R.; Liu, X.; You, J. The role of strain in oxygen evolution reaction. *J. Energy Chem.* **2024**, 93, 322–344.
- (19) Xu, X.; Liang, T.; Kong, D.; Wang, B.; Zhi, L. Strain engineering of two-dimensional materials for advanced electrocatalysts. *Mater. Today Nano* **2021**, *14*, 100111.
- (20) Yang, X.; Wang, Y.; Tong, X.; Yang, N. Strain engineering in electrocatalysts: Fundamentals, progress, and perspectives. *Adv. Energy Mater.* **2022**, *12*, 2102261.
- (21) Lin, J.; Zhang, N. Constructing strain in electrocatalytic materials for CO_2 reduction reactions. *Green. Chem.* **2024**, 26, 4449–4467.
- (22) Deng, Q.; Xu, P.; Gomaa, H.; Shenashen, M. A.; El-Safty, S. A.; An, C.; Shao, L.-H.; Hu, N. Strain engineering in electrocatalysis: Strategies, characterization, and insights. *Nano Res.* **2024**, *17*, 3603–3621
- (23) Hou, Z.; Cui, C.; Li, Y.; Gao, Y.; Zhu, D.; Gu, Y.; Pan, G.; Zhu, Y.; Zhang, T. Lattice-Strain Engineering for Heterogenous Electrocatalytic Oxygen Evolution Reaction. *Adv. Mater.* **2023**, *35*, 2209876.
- (24) He, T.; Wang, W.; Shi, F.; Yang, X.; Li, X.; Wu, J.; Yin, Y.; Jin, M. Mastering the surface strain of platinum catalysts for efficient electrocatalysis. *Nature* **2021**, *598*, 76–81.
- (25) Li, M.; Zhao, Z.; Xia, Z.; Luo, M.; Zhang, Q.; Qin, Y.; Tao, L.; Yin, K.; Chao, Y.; Gu, L.; et al. Exclusive strain effect boosts overall water splitting in PdCu/Ir core/shell nanocrystals. *Angew. Chem., Int. Ed.* **2021**, *60*, 8243–8250.
- (26) Zhuang, L.; Jia, Y.; Liu, H.; Wang, X.; Hocking, R. K.; Liu, H.; Chen, J.; Ge, L.; Zhang, L.; Li, M.; et al. Defect-induced Pt-Co-Se coordinated sites with highly asymmetrical electronic distribution for boosting oxygen-involving electrocatalysis. *Adv. Mater.* **2019**, *31*, 1805581.
- (27) Jiang, K.; Luo, M.; Liu, Z.; Peng, M.; Chen, D.; Lu, Y.-R.; Chan, T.-S.; de Groot, F. M. F.; Tan, Y. Rational strain engineering of single-atom ruthenium on nanoporous MoS₂ for highly efficient hydrogen evolution. *Nat. Commun.* **2021**, *12*, 1687.
- (28) Kim, J.; Shih, P.-C.; Tsao, K.-C.; Pan, Y.-T.; Yin, X.; Sun, C.-J.; Yang, H. High-performance pyrochlore-type yttrium ruthenate electrocatalyst for oxygen evolution reaction in acidic media. *J. Am. Chem. Soc.* **2017**, *139*, 12076–12083.
- (29) Kim, J.; Yin, X.; Tsao, K. C.; Fang, S.; Yang, H. $Ca_2Mn_2O_5$ as oxygen-deficient perovskite electrocatalyst for oxygen evolution reaction. *J. Am. Chem. Soc.* **2014**, *136*, 14646–14649.
- (30) Shi, Y.; Lyu, Z.; Zhao, M.; Chen, R.; Nguyen, Q. N.; Xia, Y. Noble-metal nanocrystals with controlled shapes for catalytic and electrocatalytic applications. *Chem. Rev.* **2021**, *121*, 649–735.
- (31) Hao, S.; Sheng, H.; Liu, M.; Huang, J.; Zheng, G.; Zhang, F.; Liu, X.; Su, Z.; Hu, J.; Qian, Y.; et al. Torsion strained iridium oxide for efficient acidic water oxidation in proton exchange membrane electrolyzers. *Nat. Nanotechnol.* **2021**, *16*, 1371–1377.
- (32) Chattot, R.; Asset, T.; Bordet, P.; Drnec, J.; Dubau, L.; Maillard, F. Beyond strain and ligand effects: Microstrain-induced enhancement of the oxygen reduction reaction kinetics on various PtNi/C nanostructures. ACS Catal. 2017, 7, 398–408.
- (33) Mariano, R. G.; McKelvey, K.; White, H. S.; Kanan, M. W. Selective increase in CO₂ electroreduction activity at grain-boundary surface terminations. *Science* **2017**, 358, 1187–1192.
- (34) Kim, J.; Chen, X.; Shih, P.-C.; Yang, H. Porous perovskite-type lanthanum cobaltite as electrocatalysts toward oxygen evolution reaction. *ACS Sustain. Chem. Eng.* **2017**, *5*, 10910–10917.
- (35) Kim, J.; Shih, P.-C.; Qin, Y.; Al-Bardan, Z.; Sun, C.-J.; Yang, H. A porous pyrochlore $Y_2[Ru_{1.6}Y_{0.4}]O_{7-\delta}$ electrocatalyst for enhanced performance towards the oxygen evolution reaction in acidic media. *Angew. Chem., Int. Ed.* **2018**, *57*, 13877–13881.

- (36) Wang, F.; Zhang, C.; Yang, H. Mixed B-site ruddlesden-popper phase $Sr_2(Ru_xIr_{1-x})O_4$ enables enhanced activity for oxygen evolution reaction. *J. Energy Chem.* **2022**, *70*, 623–629.
- (37) Zhang, C.; Wang, F.; Batool, M.; Xiong, B.; Yang, H. Phase transition of SrCo_{0.9}Fe_{0.1}O₃ electrocatalysts and their effects on oxygen evolution reaction. *SusMater.* **2022**, *2*, 445–455.
- (38) Zhang, C.; Wang, F.; Xiong, B.; Yang, H. Regulating the electronic structures of mixed B-site pyrochlore to enhance the turnover frequency in water oxidation. *Nano Convergence* **2022**, *9*, 22.
- (39) Qin, Y.; Yu, T.; Deng, S.; Zhou, X.-Y.; Lin, D.; Zhang, Q.; Jin, Z.; Zhang, D.; He, Y.-B.; Qiu, H.-J.; et al. RuO₂ electronic structure and lattice strain dual engineering for enhanced acidic oxygen evolution reaction performance. *Nat. Commun.* **2022**, *13*, 3784.
- (40) Sun, L.; Dai, Z.; Zhong, L.; Zhao, Y.; Cheng, Y.; Chong, S.; Chen, G.; Yan, C.; Zhang, X.; Tan, H.; et al. Lattice strain and atomic replacement of CoO₆ octahedra in layered sodium cobalt oxide for boosted water oxidation electrocatalysis. *Appl. Catal. B Environ.* **2021**, 297, 120477.
- (41) Hou, Z.; Sun, Z.; Cui, C.; Zhu, D.; Yang, Y.; Zhang, T. Ru coordinated ZnIn₂S₄ triggers local lattice-strain engineering to endow high-efficiency electrocatalyst for advanced Zn-air batteries. *Adv. Funct. Mater.* **2022**, 32, 2110572.
- (42) Kim, J.; Chen, X.; Pan, Y.-T.; Shih, P.-C.; Yang, H. W-doped CaMnO_{2.5} and CaMnO₃ electrocatalysts for enhanced performance in oxygen evolution and reduction reactions. *J. Electrochem. Soc.* **2017**, *164*. F1074.
- (43) Liu, D.; Luo, D.; Iqbal, A. N.; Orr, K. W. P.; Doherty, T. A. S.; Lu, Z.-H.; Stranks, S. D.; Zhang, W. Strain analysis and engineering in halide perovskite photovoltaics. *Nat. Mater.* **2021**, *20*, 1337–1346.
- (44) Perivoliotis, D. K.; Ekspong, J.; Zhao, X.; Hu, G.; Wågberg, T.; Gracia-Espino, E. Recent progress on defect-rich electrocatalysts for hydrogen and oxygen evolution reactions. *Nano Today* **2023**, *50*, 101883.
- (45) Yan, X.; Zhuang, L.; Zhu, Z.; Yao, X. Defect engineering and characterization of active sites for efficient electrocatalysis. *Nanoscale* **2021**, *13*, 3327–3345.
- (46) Smith, A. M.; Mohs, A. M.; Nie, S. Tuning the optical and electronic properties of colloidal nanocrystals by lattice strain. *Nat. Nanotechnol.* **2009**, *4*, 56–63.
- (47) Khorshidi, A.; Violet, J.; Hashemi, J.; Peterson, A. A. How strain can break the scaling relations of catalysis. *Nat. Catal.* **2018**, *1*, 263–268.
- (48) He, Y.; Shi, Q.; Shan, W.; Li, X.; Kropf, A. J.; Wegener, E. C.; Wright, J.; Karakalos, S.; Su, D.; Cullen, D. A.; et al. Dynamically unveiling metal-nitrogen coordination during thermal activation to design high-efficient atomically dispersed CoN₄ active sites. *Angew. Chem., Int. Ed.* **2021**, *60*, 9516–9526.
- (49) Gao, G.; Sun, Z.; Chen, X.; Zhu, G.; Sun, B.; Yamauchi, Y.; Liu, S. Recent advances in Ru/Ir-based electrocatalysts for acidic oxygen evolution reaction. *Appl. Catal. B Environ.* **2024**, 343, 123584.
- (50) Higareda, A.; Hernández-Arellano, D. L.; Ordoñez, L. C.; Barbosa, R.; Alonso-Vante, N. Advanced electrocatalysts for the oxygen evolution reaction: From single- to multielement materials. *Catalysts* **2023**, *13*, 1346.
- (51) Mavrikakis, M.; Hammer, B.; Nørskov, J. K. Effect of strain on the reactivity of metal surfaces. *Phys. Rev. Lett.* **1998**, *81*, 2819–2822.
- (52) Sun, Y.; Liang, Y.; Luo, M.; Lv, F.; Qin, Y.; Wang, L.; Xu, C.; Fu, E.; Guo, S. Defects and interfaces on PtPb nanoplates boost fuel cell electrocatalysis. *Small* **2018**, *14*, 1702259.
- (53) Li, C.; Yuan, Q.; Ni, B.; He, T.; Zhang, S.; Long, Y.; Gu, L.; Wang, X. Dendritic defect-rich palladium-copper-cobalt nanoalloys as robust multifunctional non-platinum electrocatalysts for fuel cells. *Nat. Commun.* **2018**, *9*, 3702.
- (54) Hu, X.; Zou, J.; Gao, H.; Kang, X. Trimetallic Ru@AuPt coreshell nanostructures: The effect of microstrain on CO adsorption and electrocatalytic activity of formic acid oxidation. *J. Colloid Interface Sci.* **2020**, *570*, 72–79.
- (55) Yang, F.; Elnabawy, A. O.; Schimmenti, R.; Song, P.; Wang, J.; Peng, Z.; Yao, S.; Deng, R.; Song, S.; Lin, Y.; et al. Bismuthene for

- highly efficient carbon dioxide electroreduction reaction. *Nat. Commun.* **2020**, *11*, 1088.
- (56) Hao, J.; Zhuang, Z.; Hao, J.; Cao, K.; Hu, Y.; Wu, W.; Lu, S.; Wang, C.; Zhang, N.; Wang, D.; et al. Strain relaxation in metal alloy catalysts steers the product selectivity of electrocatalytic CO₂ reduction. *ACS Nano* **2022**, *16*, 3251–3263.
- (57) Mao, X.; Qin, Z.; Ge, S.; Rong, C.; Zhang, B.; Xuan, F. Strain engineering of electrocatalysts for hydrogen evolution reaction. *Mater. Horiz.* **2023**, *10*, 340–360.
- (58) Yang, Y.; Jia, Z.; Wang, Q.; Liu, Y.; Sun, L.; Sun, B.; Kuang, J.; Dai, S.; He, J.; Liu, S.; et al. Vacancy induced microstrain in highentropy alloy film for sustainable hydrogen production under universal pH conditions. *Energy Environ. Sci.* **2024**, *17*, 5854–5865.
- (59) Guo, H.; Li, L.; Chen, Y.; Zhang, W.; Shang, C.; Cao, X.; Li, M.; Zhang, Q.; Tan, H.; Nie, Y.; et al. Precise Strain Tuning Boosts Electrocatalytic Hydrogen Generation. *Adv. Mater.* **2023**, *35*, 2302285.
- (60) Hua, Q.; Chen, X.; Chen, J.; Alghoraibi, N. M.; Lee, Y.; Woods, T. J.; Haasch, R. T.; Zimmerman, S. C.; Gewirth, A. A. Inducing microstrain in electrodeposited Pt through polymer addition for highly active oxygen reduction catalysis. *ACS Catal.* **2024**, *14*, 7526–7535.
- (61) Zhao, X.; Takao, S.; Yoshida, Y.; Kaneko, T.; Gunji, T.; Higashi, K.; Uruga, T.; Iwasawa, Y. Roles of structural defects in polycrystalline platinum nanowires for enhanced oxygen reduction activity. *Appl. Catal. B Environ.* **2023**, 324, 122268.
- (62) Lu, X.; Ahmadi, M.; DiSalvo, F. J.; Abruña, H. D. Enhancing the electrocatalytic activity of Pd/M (M = Ni, Mn) nanoparticles for the oxygen reduction reaction in alkaline media through electrochemical dealloying. *ACS Catal.* **2020**, *10*, 5891–5898.
- (63) Chen, Y.; Sun, M.; Wu, M.; Zhu, C.; Li, H.; Lin, Z.-Y.; Li, H.; Xu, H.; Li, D.; Chen, X.; et al. Enhancing oxygen reduction activity via tailoring microstrain in PdMo nanoalloy through repetitive hydrogen absorption-release. *ACS Catal.* **2024**, *14*, 9354–9363.
- (64) Wang, L.; Zeng, Z.; Gao, W.; Maxson, T.; Raciti, D.; Giroux, M.; Pan, X.; Wang, C.; Greeley, J. Tunable intrinsic strain in two-dimensional transition metal electrocatalysts. *Science* **2019**, 363, 870–874
- (65) Li, Z.; Wang, Q.; Bai, X.; Wang, M.; Yang, Z.; Du, Y.; Sterbinsky, G. E.; Wu, D.; Yang, Z.; Tian, H.; et al. Doping-modulated strain control of bifunctional electrocatalysis for rechargeable zinc-air batteries. *Energy Environ. Sci.* **2021**, *14*, 5035–5043.
- (66) Wang, P.; Zhao, R.; Zhang, F.; Wang, J.; Han, B.; Liu, Z. Interface engineered Co, Ni, Fe, Cu oxide hybrids with biphasic structures for water splitting with enhanced activity. *J. Colloid Interface Sci.* **2022**, 609, 149–157.
- (67) Zhang, X.; Zhang, J.; Xu, B.; Wang, K.; Sun, X. W. Synergistic effects in biphasic nanostructured electrocatalyst: Crystalline core versus amorphous shell. *Nano Energy* **2017**, *41*, 788–797.
- (68) Zhang, Q.; Liu, T.; Guo, H.; Chen, Y.; Di, Y.; Zhang, Z.; Wang, F. Lead-induced microstrain in synthesis and manipulation of porous pyrochlore for boosting oxygen evolution reaction. *Adv. Funct. Mater.* **2024**, *34*, 2306176.
- (69) Wang, Y.; Jiao, Y. Q.; Yan, H. J.; Yang, G. C.; Tian, C. G.; Wu, A. P.; Liu, Y.; Fu, H. G. Vanadium-incorporated CoP with lattice expansion for highly efficient acidic overall water splitting. *Angew. Chem., Int. Ed.* **2022**, *61*, No. e202116233.
- (70) Zhou, P.; Zhai, G. Y.; Lv, X. S.; Liu, Y. Y.; Wang, Z. Y.; Wang, P.; Zheng, Z. K.; Cheng, H. F.; Dai, Y.; Huang, B. B. Boosting the electrocatalytic HER performance of Ni₃N-V₂O₃ via the interface coupling effect. *Appl. Catal. B Environ.* **2021**, 283, 119590.
- (71) Cheng, Z. H.; Xiao, Y. K.; Wu, W. P.; Zhang, X. Q.; Fu, Q.; Zhao, Y.; Qu, L. T. All-pH-tolerant in-plane heterostructures for efficient hydrogen evolution reaction. *ACS Nano* **2021**, *15*, 11417–11427.
- (72) Xing, M. H.; Qiao, Z. L.; Niu, Z. Q.; Wang, S. T.; Liu, Z. P.; Cao, D. P. Strain engineering of the NiTe/NiP heterostructure to boost the oxygen evolution reaction. *ACS Appl. Mater. Interfaces* **2023**, 15, 40428–40437.

- (73) Williamson, G. K.; Hall, W. H. X-ray line broadening from filed aluminium and wolfram. *Acta Metall.* **1953**, *1*, 22–31.
- (74) Khorsand Zak, A.; Abd. Majid, W. H.; Abrishami, M. E.; Yousefi, R. X-ray analysis of ZnO nanoparticles by Williamson-Hall and size-strain plot methods. *Solid State Sci.* **2011**, *13*, 251–256.
- (75) Rietveld, H. M. A profile refinement method for nuclear and magnetic structures. *J. Appl. Crystallogr.* **1969**, *2*, 65–71.
- (76) Schultz, Z. D.; Feng, Z. V.; Biggin, M. E.; Gewirth, A. A. Vibrational spectroscopic and mass spectrometric studies of the interaction of bis(3-sulfopropyl)-disulfide with Cu surfaces. *J. Electrochem. Soc.* **2006**, *153*, C97.
- (77) Mote, V. D.; Purushotham, Y.; Dole, B. N. Williamson-Hall analysis in estimation of lattice strain in nanometer-sized ZnO particles. *J. Theor. Appl. Phys.* **2012**, *6*, 6.
- (78) Patterson, A. L. The Scherrer formula for X-Ray particle size determination. *Phys. Rev.* **1939**, *56*, 978–982.
- (79) Tagliente, M. A.; Massaro, M. Strain-driven (002) preferred orientation of ZnO nanoparticles in ion-implanted silica. *Nucl. Instrum. Methods Phys. Res., B* **2008**, 266, 1055–1061.
- (80) Hÿtch, M. J.; Snoeck, E.; Kilaas, R. Quantitative measurement of displacement and strain fields from HREM micrographs. *Ultramicroscopy* **1998**, *74*, 131–146.
- (81) Crecelius, G.; Wertheim, G. K.; Buchanan, D. N. E. Core-hole screening in lanthanide metals. *Phys. Rev. B* **1978**, *18*, 6519–6524.
- (82) Lütkehoff, S.; Neumann, M.; Ślebarski, A. 3d and 4d x-ray-photoelectron spectra of Pr under gradual oxidation. *Phys. Rev. B* **1995**, *52*, 13808–13811.
- (83) Hatch, R. C.; Fredrickson, K. D.; Choi, M.; Lin, C.; Seo, H.; Posadas, A. B.; Demkov, A. A. Surface electronic structure for various surface preparations of Nb-doped SrTiO₃ (001). *J. Appl. Phys.* **2013**, *114*, 103710.
- (84) Feng, X.; Cox, D. F. Oxidation of MnO(100) and $NaMnO_2$ formation: Characterization of Mn^{2+} and Mn^{3+} surfaces via XPS and water TPD. Surf. Sci. 2018, 675, 47–53.
- (85) Zhang, Y.; Gao, X.; Weaver, M. J. Nature of surface bonding on voltammetrically oxidized noble metals in aqueous media as probed by real-time surface-enhanced Raman spectroscopy. *J. Phys. Chem.* **1993**, *97*, 8656–8663.
- (86) Yu, A.; Rizo, R.; Vidal-Iglesias, F. J.; Arán-Ais, R. M.; Chen, Y.-X.; Herrero, E.; Feliu, J. M. The surface processes on Ru/Pt(111) as probed by cyclic voltammetry and in situ surface-enhanced Raman spectroscopy. *ACS Sustain. Chem. Eng.* **2022**, *10*, 14826–14834.
- (87) Henderson, S. J.; Shebanova, O.; Hector, A. L.; McMillan, P. F.; Weller, M. T. Structural variations in pyrochlore-structured $Bi_2Hf_2O_7$, $Bi_2Ti_2O_7$ and $Bi_2Hf_2_xTi_xO_7$ solid solutions as a function of composition and temperature by neutron and X-ray diffraction and Raman spectroscopy. *Chem. Mater.* **2007**, *19*, 1712–1722.
- (88) Hao, J.; Xu, Z.; Han, M.-J.; Xu, S.; Meng, X. Surface-enhanced Raman scattering analysis of perchlorate using silver nanofilms deposited on copper foils. *Colloids Surf., A* **2010**, *366*, 163–169.
- (89) Bae, J. S.; Yang, I. S.; Lee, J. S.; Noh, T. W.; Takeda, T.; Kanno, R. Raman scattering study of the geometrically frustrated pyrochlore $Y_2Ru_2O_7$. Vib. Spectrosc. **2006**, 42, 284–287.
- (90) Chan, H. Y. H.; Takoudis, C. G.; Weaver, M. J. High-pressure oxidation of ruthenium as probed by surface-enhanced Raman and X-ray photoelectron spectroscopies. *J. Catal.* **1997**, *172*, 336–345.
- (91) Vandenborre, M. T.; Husson, E.; Chatry, J. P.; Michel, D. Rareearth titanates and stannates of pyrochlore structure vibrational-spectra and force-fields. *J. Raman. Spectrosc.* **1983**, *14*, 63–71.
- (92) Luo, H.; Park, S.; Chan, H. Y. H.; Weaver, M. J. Surface oxidation of platinum-group transition metals in ambient gaseous environments: Role of electrochemical versus chemical pathways. *J. Phys. Chem. B* **2000**, *104*, 8250–8258.
- (93) Chattot, R.; Le Bacq, O.; Beermann, V.; Kühl, S.; Herranz, J.; Henning, S.; Kühn, L.; Asset, T.; Guétaz, L.; Renou, G.; et al. Surface distortion as a unifying concept and descriptor in oxygen reduction reaction electrocatalysis. *Nat. Mater.* **2018**, *17*, 827–833.
- (94) Kühl, S.; Gocyla, M.; Heyen, H.; Selve, S.; Heggen, M.; Dunin-Borkowski, R. E.; Strasser, P. Concave curvature facets benefit oxygen

- electroreduction catalysis on octahedral shaped PtNi nanocatalysts. J. Mater. Chem. A 2019, 7, 1149-1159.
- (95) Chattot, R.; Martens, I.; Scohy, M.; Herranz, J.; Drnec, J.; Maillard, F.; Dubau, L. Disclosing Pt-bimetallic alloy nanoparticle surface lattice distortion with electrochemical probes. *ACS Energy Lett.* **2020**, *5*, 162–169.

